

Classical-linear-chain behavior from dipolar droplets to supersolidsK. Mukherjee  and S. M. Reimann*Mathematical Physics and NanoLund, LTH, Lund University, Box 118, 22100 Lund, Sweden* (Received 21 December 2022; revised 4 March 2023; accepted 10 April 2023; published 24 April 2023)

We investigate the classicality of linear dipolar droplet arrays through a normal mode analysis of the dynamical properties in comparison to the supersolid regime. The vibrational patterns of isolated-droplet crystals that time-evolve after a small initial kick closely follow the properties of a linear droplet chain. For larger kick velocities, however, droplets may coalesce and separate again, showing distinct deviations from classicality. In the supersolid regime the normal modes are eliminated by a counterflow of mass between the droplets, signaled by a reduction of the center-of-mass motion. Our study effectively captures the vibrational patterns of isolated droplets in the presence of three-body loss and can be generalized to systems with a larger number of droplet arrays.

DOI: [10.1103/PhysRevA.107.043319](https://doi.org/10.1103/PhysRevA.107.043319)**I. INTRODUCTION**

In dipolar Bose-Einstein condensates (dBEC) intriguing new quantum phases of matter at ultra-low temperatures were discovered (see, e.g., the reviews [1–5]). Remarkably, a trapped dBEC can develop a spontaneous periodic density modulation while maintaining coherence and frictionless flow, resulting in a dipolar supersolid [6–13]. Such a state of matter with simultaneous off-diagonal and diagonal long-range order [14–20] has long been debated for ^4He [20–24], followed by alternative setups with ultra-cold atoms [25–31]. In dBECs, the mechanism driving the formation of broken-symmetry states originates from the interplay between interparticle interactions and quantum fluctuations [32–34]. In experiments with dysprosium [35–38] or erbium [39,40] it was found that density modulations and self-bound filaments stabilize similarly to droplets of binary Bose gases [41–43] realized with potassium in different hyperfine states [44–46]. The dBEC includes both short- and long-range interactions, and by increasing the relative strength of the long-range interaction, there is a transition from a superfluid to a supersolid and a crystal phase where the droplets become almost isolated from one another [33,47]. In addition to the above references there is a large volume of works addressing dipolar droplets and supersolids, see, for example, [13,34,47–73]. Dipolar mixtures [74–79] were also discussed. Recent experimental efforts are directed towards two-dimensional systems, see, e.g., [65,80–82] and vorticity [83], and to explore the out-of-equilibrium dynamics [10,82,84–86].

While the underlying origin of the self-bound droplets is purely quantum mechanical, there is an aspect of *classicality*.

The droplets may localize and rigidly organize themselves in lattice-periodic structures. Alternatively, they may phase-coherently overlap, forming a supersolid. An intriguing and unresolved question is to what extent classicality may prevail in these systems. In this article, we demonstrate a mechanism to gauge the classicality of these supersolid or droplet array states by their dynamics, based on a classical linear-chain model [87,88] in comparison to a dynamical Gross-Pitaevskii (eGP) approach. We consider a few droplets in a dBEC confined by a three-dimensional elongated harmonic trap [see Fig. 1(a)], similar to the recent experiments in [6–8,12,13]. To initiate the vibrational dynamics, we give one or two droplets a kick along the weakly confined direction, as sketched in Fig. 1(b). Remarkably, a classical spring-mass model as sketched in Fig. 1(c) can perfectly account for the vibrational patterns, provided the droplets are fully separated from each other. The observed vibrational frequencies hint at the triggering of underlying collective excitation modes [12,13]. A finite background density interconnecting the droplets, however, destroys the resemblance to classical patterns by inducing particle flow between the droplets. When the kick velocity is large enough compared to the velocity scale imposed by the harmonic confinement, droplets that are initially isolated can collide, transferring particles from outer to central droplets, a phenomenon that mimics the collision of classical liquid droplets [89,90]. This collision destroys the above-mentioned vibrational pattern as well. It is worth noting that the normal modes of vibration of soliton molecules in a dipolar condensate under the influence of disturbances was also discussed in [91–93]. For binary quantum droplets with short-range interactions [44,45] collision dynamics previously was reported in experiment [94] and theory [95,96]. In contrast, in the present work the collision dynamics between droplets is realized within a single confined species. Our findings offer an avenue to assess classicality and the dynamical manifestation of collective excitations in droplet arrays at the verge between the crystal and supersolid phase.

Published by the American Physical Society under the terms of the Creative Commons Attribution 4.0 International license. Further distribution of this work must maintain attribution to the author(s) and the published article's title, journal citation, and DOI. Funded by Bibsam.

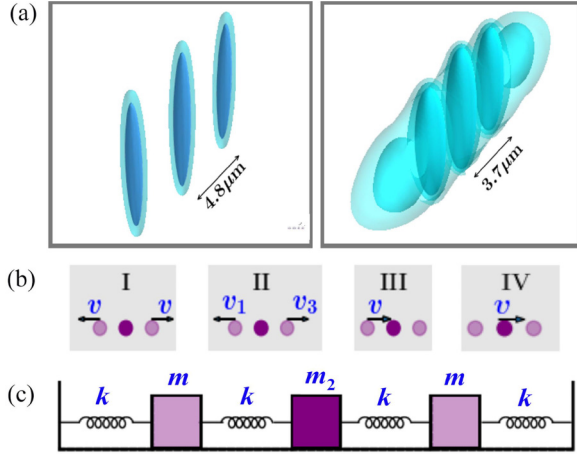


FIG. 1. (a) Isosurfaces of three-dimensional density depicting isolated droplets (left) and a supersolid phase (right), realized by a system of $N = 35\,000$ ^{164}Dy atoms at scattering length $a = 84a_0$ and $a = 94a_0$, respectively. (b) Sketch of different configurations where one or two droplets are kicked with a velocity. (c) Sketch of the linear chain model of the linear droplet array, with masses m and m_2 attached by springs of stiffness k .

The structure of our paper is organized as follows. In Sec. II, we introduce the relevant theoretical framework, the velocity configurations employed, and the experimentally relevant parameters of our setup. We then proceed to present the emergence of vibrational patterns of isolated droplets following an initial kick in Sec. III and discuss the normal mode analysis in Sec. IV. The vibrational patterns within the supersolid state are showcased in Sec. V. We analyze the influence of three-body losses on the vibrational patterns of the isolated droplets in Sec. VI. In Sec. VII, we summarize our findings and provide an outlook on future perspectives. Additionally, we provide further elaboration on the details of the utilized beyond mean-field framework and the ingredients of the presented simulations in Appendix A. A detailed derivation of the normal mode frequencies is provided in Appendix B. Finally, Appendix C displays the vibrational dynamics of five isolated droplets.

II. MODEL AND METHODS

We consider a dBEC of atoms with mass M and magnetic dipole moment μ aligned along the z axis, harmonically trapped by $V(r) = M(\omega_x^2 x^2 + \omega_y^2 y^2 + \omega_z^2 z^2)/2$. The frequencies ω_i (where $i = x, y, z$) satisfy $\omega_x < \omega_y, \omega_z$ resulting in an elongated geometry along x . At zero temperature, the system is well described by the eGP equation [32,33,39]

$$i\hbar \frac{\partial \psi(\mathbf{r}, t)}{\partial t} = \left[-\frac{\hbar^2}{2M} \nabla^2 + V(\mathbf{r}) + g|\psi(\mathbf{r}, t)|^2 + \gamma(\epsilon_{dd})|\psi(\mathbf{r}, t)|^3 + \int d\mathbf{r}' U_{dd}(\mathbf{r} - \mathbf{r}') |\psi(\mathbf{r}', t)|^2 \right] \psi(\mathbf{r}, t), \quad (1)$$

where $g = 4\pi\hbar^2 a/M$ is the short-range repulsive contact interaction fixed by the scattering length a and the dipolar

interaction $U_{dd}(\mathbf{r}, t) = \frac{\mu_0 \mu_m^2}{4\pi} \left[\frac{1-3\cos^2\theta}{r^3} \right]$ with θ being the angle between \mathbf{r} and the z axis. The final term in Eq. (1) is given by the repulsive Lee-Huang-Yang (LHY) correction with $\gamma(\epsilon_{dd}) = \frac{32}{3} g \sqrt{\frac{a^3}{\pi}} \left(1 + \frac{3}{2} \epsilon_{dd}^2 \right)$ [32,97]. The dimensionless parameter $\epsilon_{dd} = a_{dd}/a$ with dipolar length $a_{dd} = \mu_0 \mu_m^2 M / 12\pi \hbar^2$ quantifies the relative strength of the DDI as compared to the contact interaction and $v_{\text{osc}} = \sqrt{\hbar\omega_x/M}$ sets the characteristic harmonic oscillator velocity scale. Equation (1) is solved using a split-step Crank-Nicholson method [98,99] in imaginary time to obtain the initial ground state and in real time to monitor the dynamics (see Appendix A for details). The system showcases a superfluid phase for a sufficiently small value of ϵ_{dd} . Increasing this parameter, the supersolid phase (SS) is favored in a window of values of ϵ_{dd} beyond which one enters the isolated droplet phase (DL₁).

In the following, we utilize the experimentally relevant [6,7] parameters of ^{164}Dy dipolar BEC, namely, $\omega_x/(2\pi) = 19\text{Hz}$, $\omega_y/(2\pi) = 53\text{Hz}$, and $\omega_z/(2\pi) = 81\text{Hz}$, and $N = 35\,000$. Modulated density profiles are found for $a < 94.9a_0$. The density isosurfaces of the DL₁ and SS phases, realized at $a = 84a_0$ and $94a_0$, respectively, are shown in Fig. 1(a). Having determined the ground state, showing the three localized density structures (droplets), we investigate the vibrational and collisional dynamics of these dipolar droplets. To accomplish this, we give a specific droplet an initial kick with velocity v at $t = 0$ in the following manner. First, the central position (x_0) of a droplet along the x axis in SS and DL₁ phases is determined by locating the peaks in the ground-state density profiles. Then we apply a quench through a transformation of the order parameter

$$\psi(x, y, z) = \psi(x, y, z) e^{iv\mathcal{F}(x)}. \quad (2)$$

Here, the function $\mathcal{F}(x) = A/\{A + B \cosh[L(x - x_0)]\}$, with A, B , and L being constants, guarantees that each localized droplet has velocity v across its spatial extent; beyond its extent the velocity falls to zero swiftly but continuously, maintaining the continuity of the wave function (see Appendix A). Depending upon which droplets are being kicked and the initial conditions thereof, a variety of dynamical situations can be realized. We consider the following four cases [see Fig. 1(b)]. Case I corresponds to kicking the left and right droplets with equal velocity in the $-x$ and $+x$ directions, respectively. In case II, the left and right droplets are kicked in the opposite direction with unequal velocity. Case III constitutes the left droplet being kicked in the $+x$ direction. Finally, case IV deals with the scenario where only the central droplet is kicked in the $+x$ direction.

III. VIBRATIONAL AND COLLISIONAL DYNAMICS

To elucidate the vibrational and collisional dynamics taking place along the weakly confined x direction, we examine the time evolution of the one-dimensional (1D) integrated density profiles, with $n_{1D}(x) = \int |\psi(x, y, z)|^2 dy dz$ being experimentally detectable, e.g., via *in situ* imaging [5,13]. Focusing first on case I [Figs. 2(a₁) to 2(a₃)], we notice that the outer droplets exhibit periodic vibrational motion, while the center droplet stays motionless. For low-enough velocity, $v < v_{\text{osc}}$ [Fig. 2(a₁)], the motion is precisely of sinusoidal

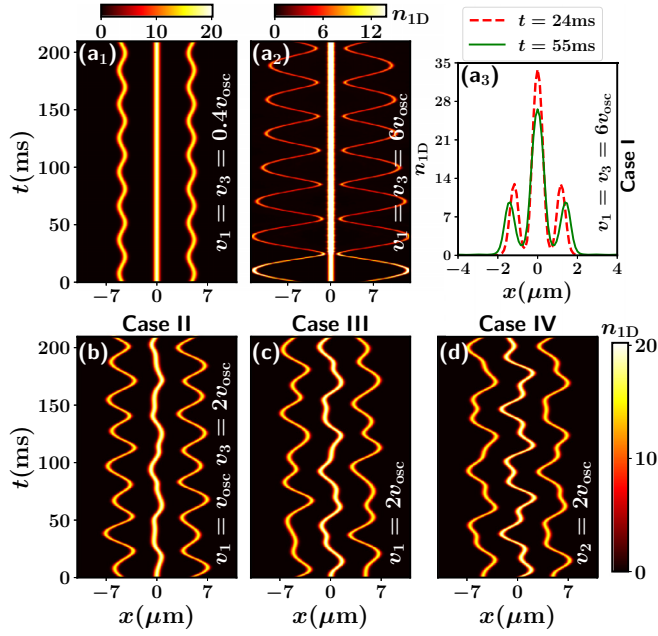


FIG. 2. Time evolution of integrated density n_{1D} of quasi-one-dimensional (1D) dipolar quantum droplets exhibiting (a₁) pure vibrational and (a₂) collisional dynamics for the case **I** when two outer droplets are kicked in the opposite direction with the same velocity (see the legends). (a₃) The integrated density profiles n_{1D} during the first two collision times corresponding to (a₂). During the collision, the droplets make direct contact, exchanging particles from the outside to the central droplet [(a₂), (a₃)]. Shown also in the vibrational dynamics within (b) case **II**, (c) case **III**, and (d) case **IV** that feature different initial velocity configurations (see also the legends). The colorbar represents 1D density n_{1D} in the unit of $1000 \mu\text{m}^{-1}$. The colorbar in (a₂) has been adjusted to enhance the contrast. The $v_{\text{osc}} = 2.1 \times 10^{-4} \text{ m/s}$ is the characteristic harmonic oscillator velocity scale.

type with a π phase difference between the trajectories of the left and right droplets. This resembles a fundamental mode of vibration of a corresponding *classical* spring-mass system (see the discussion below). The amplitude of vibration increases for increasing velocity $v > v_{\text{osc}}$, and the two outer droplets can collide with the central one, resulting in particle exchange either from the outer droplets to the central one or vice versa. For example, a particle transfer from the outer to central droplet upon collision can be noticed [Fig. 2(a₂)] when $v_1 = v_3 = 6v_{\text{osc}}$. Note that a particle exchange occurs exclusively during the first two direct encounters between droplets at $t \approx 24 \text{ ms}$ and $t \approx 55 \text{ ms}$, respectively. For $t > 55 \text{ ms}$, the amplitude of vibration of the outer droplets decreases, and as a result, they no longer come into direct contact with the central droplet, with no further collisions. We stress that, while the total momentum of the system is conserved for the considered case **I**, each droplet, via mass transfer, shares an equal magnitude but opposite sign of momentum to the central droplet. As a result, the interactions between droplets change, leading to a decrease in the oscillatory amplitude. To better resolve the collision, we also show in Fig. 2(a₃) the density profiles n_{1D} at $t = 24 \text{ ms}$ and $t = 55 \text{ ms}$, respectively. Evidently, the droplets overlap during the collision, causing

mass-flow. Consequently, the vibrational mode visible at low kick velocity [see, for example, Fig. 2(a₂)] is eliminated.

Interestingly, for $v_1 \neq v_3$ (case **II**), the central droplet ceases to be stationary, see Fig. 2(b), signaling the onset of center-of-mass (COM) motion. Also, the trajectory of each droplet is not purely sinusoidal anymore. This suggests that the emerging vibration is not caused just by a single fundamental mode but rather by a linear combination of different modes. A very similar dynamics is observed for case **III**. The representative example illustrated in Fig. 2(c) indicates the involvement of multiple frequencies in the vibrational pattern. Now, the left droplet receives a kick along the $+x$ direction and it moves until it reaches the close vicinity of the central one at $t = 7.5 \text{ ms}$. The central droplet then begins to migrate toward the right one, compelling the latter to move in the $+x$ direction as well. Turning to the case **IV** [Fig. 2(d)], when the central droplet is kicked towards the right one, we notice that the outer droplets follow nearly identical trajectories, vibrating in phase, while the central one showcases out-of-phase vibration with the others, in contrast to the cases mentioned before. This drastic modification of the vibrational pattern arguably hints at the vanishing or softening of the fundamental mode responsible for the dynamics of case **I**, setting the stage for analyzing the system in terms of its classical modes.

IV. NORMAL MODES OF VIBRATION

To capture the fundamental modes of vibration responsible for the emergent oscillation pattern observed in the eGP simulation, we resort to the so-called normal mode analysis (NMA) [87]. In particular, we model the three harmonically localized droplets as three compact masses connected by springs with spring constant k , sketched in Fig. 1(c), assuming that the well-known Hooke's law [88] is satisfied. Inspired by the eGP simulations, we assume that the central droplet has mass m_2 , while the outer ones have equal masses $m_1 = m_3 = m$. Therefore, the two characteristic angular frequencies of the springs read $\omega_1 = \sqrt{k/m}$ and $\omega_2 = \sqrt{k/m_2}$. These frequencies are determined by the combined effect of confinement and interparticle interactions. The instantaneous configuration of the system is specified by the horizontal displacements of the three masses from their equilibrium positions, $\mathbf{X}(t) = [x_1(t), x_2(t), x_3(t)]$. This is manifestly a three-degrees of freedom system, and the three normal mode frequencies (labeled from slow “s” to medium “m” to fast “f”) are given by (see Appendix B) $\omega_s = [\omega_1^2 + \omega_2^2 - \sqrt{\omega_1^4 + \omega_2^4}]^{1/2}$, $\omega_m = \sqrt{2}\omega_1$, and $\omega_f = [\omega_1^2 + \omega_2^2 + \sqrt{\omega_1^4 + \omega_2^4}]^{1/2}$, with the associated normal modes being $\mathbf{A}_1 = (\omega_1^2, 0, -\omega_1^2)$, $\mathbf{A}_2 = (\omega_1^2, \omega_2^2, \omega_1^2)$, and $\mathbf{A}_3 = (\omega_1^2, \omega_2^2, \omega_1^2)$, respectively, where $\omega_{\pm}^2 = (\omega_2^2 - \omega_1^2) \pm \sqrt{\omega_1^4 + \omega_2^4}$. Note that the initial displacements of the masses are zero, namely, $x_1(t=0) = 0$, $x_2(t=0) = 0$, and $x_3(t=0) = 0$. Consequently, the most general solution of the equation of motion, revealing trajectories of each individual mass, is given by $\mathbf{X}(t) = a_m \mathbf{A}_1 \sin(\omega_m t) + a_f \mathbf{A}_2 \sin(\omega_f t) + a_s \mathbf{A}_3 \sin(\omega_s t)$. The coefficients a_m , a_f , a_s can be found from the three initial conditions on the velocities.

For case **I**, the initial velocities read $\dot{x}_1(0) = -v$, $\dot{x}_2(0) = 0$, $\dot{x}_3(0) = v$, which give the coefficients $a_f = a_s = 0$ and $a_m = v/(\sqrt{2}\omega_1^3)$. As a result, the trajectories can be calculated

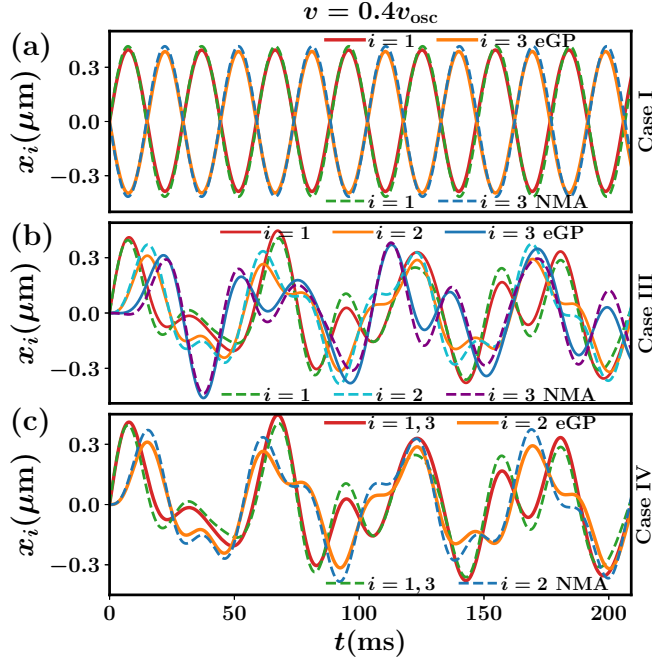


FIG. 3. Comparison of droplet trajectories $x_i(t)$ between eGP simulation and those obtained from the normal mode analysis (NMA) (see the legends) for (a) case I, (b) case III, and (c) case IV, all for velocity $v = 0.4v_{\text{osc}}$. The $v_{\text{osc}} = 2.1 \times 10^{-4}$ m/s is the characteristic harmonic oscillator velocity scale. The NMA matches well with those obtained from the eGP for the characteristic frequencies $\omega_m/(2\pi) = 33.94$ Hz, $\omega_f/(2\pi) = 46.85$ Hz, and $\omega_s/(2\pi) = 19$ Hz. The eGP simulation is performed with $N = 35000$ particles having scattering length $a = 84a_0$ and confined in a trapping potential with frequencies $\omega_x/(2\pi) = 19$ Hz, $\omega_y/(2\pi) = 53$ Hz, and $\omega_z/(2\pi) = 81$ Hz.

as $x_1(t) = a_m \sin(\omega_m t)$, $x_2(t) = 0$, and $x_3(t) = -a_m \sin(\omega_m t)$. We also calculate the trajectories of each individual droplet $x_j(t)$, with $i = 1, 3$ from the eGP simulation for the case I [see Fig. 3(a)]. For calculating the trajectory of each droplet in the extended Gross-Pitaevskii equation (eGPE) simulation, we locate the density profile of each droplet, then the trajectory is defined as $x_\sigma(t) = \int_R x |\psi(x, y, z; t)|^2 dx dy dz$. We then use the spring constant and mass in the normal mode analysis as fitting parameters to best capture the trajectory from the eGPE simulation and determine the fundamental modes of oscillation. Notably, for velocity $v < v_{\text{osc}}$, the trajectories from the simulation match perfectly to those obtained from the NMA with $\omega_m/(2\pi) = 33.94$ Hz. Indeed, the dynamics in case I is governed by one fundamental mode A_1 that causes the observed out-of-phase oscillation [Fig. 3(a)] between the left and right droplets. This also causes the overall dBEC cloud to periodically expand and contract, and thus the frequency $\omega_m/(2\pi) = 33.94$ Hz corresponds to the breathing frequency. We remark that even at large velocity $v > v_{\text{osc}}$ the mode A_1 still qualitatively explains the observed oscillation pattern although the quantitative matching between eGP and NMA improves at $v < v_{\text{osc}}$. For the initial conditions, $\dot{x}_1(0) = -v_1$, $\dot{x}_2(0) = 0$, $\dot{x}_3(0) = v_3$, with $v_1 \neq v_3$, the coefficients become $a_m = (v_3 + v_1)/(2\omega_m)$, $a_f = \omega_+^2(v_3 - v_1)/(4\omega_+^2\omega_f\sqrt{\omega_+^4 + \omega_f^4})$, and

$a_s = -\omega_-^2(v_3 - v_1)/(4\omega_+^2\omega_s\sqrt{\omega_+^4 + \omega_s^4})$. The involved oscillation frequencies in the vibrational pattern (not shown here) are given by $\omega_m/(2\pi) = 33.94$ Hz, $\omega_f/(2\pi) = 46.85$ Hz, and $\omega_s/(2\pi) = 19$ Hz. Notably, the activation of COM motion is manifested by the oscillation at $\omega_s/(2\pi) = 19$ Hz (which is equal to the trap frequency ω_x) and the relevant mode is A_3 . Naturally, a larger a_s indicates more vigorous COM motion that indeed takes place within case III having initial condition $\dot{x}_1(0) = v$, $\dot{x}_2(0) = 0$, and $\dot{x}_3(0) = 0$. The coefficients can be obtained from those of case II by substituting $v_1 = -v$ and $v_2 = 0$. The trajectories obtained via eGP simulation are well produced by those obtained via NMA [see Fig. 3(b)] with $\omega_m/(2\pi) \approx 33.94$ Hz, $\omega_f/(2\pi) \approx 46.85$ Hz, and $\omega_s/(2\pi) \approx 19$ Hz, as obtained from case II. Interestingly, the coefficient a_m vanishes for case IV while the rest become $a_f = -v/(4\omega_f\sqrt{\omega_+^4 + \omega_f^4})$ and $a_s = v/(4\omega_s\sqrt{\omega_+^4 + \omega_s^4})$, rendering $x_1(t) = x_3(t)$ and $|a_f| < |a_s|$. Thanks to the vanishing contribution of the A_1 mode, the outer droplets demonstrate the same trajectories performing in-phase oscillations and thus resulting in the strongest COM motion among the configurations considered herein. The underlying frequencies comprise of $\omega_s/(2\pi) = 19$ Hz and $\omega_f/(2\pi) = 46.85$ Hz. Thus, by maneuvering the outer droplet velocities, one can excite the single or combination of normal modes that strongly resembles those of a classical system. We note that our analysis is rather generic, applying to arrays with large numbers of isolated droplets (see [80]), different particle numbers, or trapping frequencies.

V. IMPACT OF THE SUPERSOLIDITY

The similarity of motion between the DL_I state and the conventional classical spring-mass system relies on the fact that the mass of each droplet is conserved. But Hook's law cannot adequately capture the vibrational dynamics of crystals in the supersolid state, as the droplets are connected, resulting in time-dependent mass transfer within the crystals and rendering the linear spring-mass model inapplicable. This becomes apparent from Fig. 4(a₁) where case I is displayed. Although the central droplet remains still motionless, notably there is a particle transfer across the humps via the dilute background density, even at a low velocity such as $v = 0.4v_{\text{osc}}$ [Fig. 4(a₁)]. The velocity configuration induces periodic oscillations of the density profile of the cloud, which bear the signature of two distinct breathing frequencies corresponding to the localized crystal and the background superfluidity, respectively [10]. This is in contrast to the observations in the case I configuration of the isolated droplets, where $x_1(t)$ is determined by a single breathing frequency ω_m . A notably interesting scenario emerges for case IV [Figs. 4(a₂) and 4(a₃)], depicted for two different velocities. The low-density peaks located left to the central droplet [Figs. 4(a₂) and 4(a₃)] become increasingly populated during the dynamics. This implies a mass flow along the $-x$ direction, revealing the existence of out-of-phase motion between the droplet arrays and background superfluid [11]. Furthermore, an in-phase motion exists, which corresponds to the dipole mode and determines the COM oscillation frequency of the isolated droplets. The out-of-phase motion, however, is unique to the SS state, and its

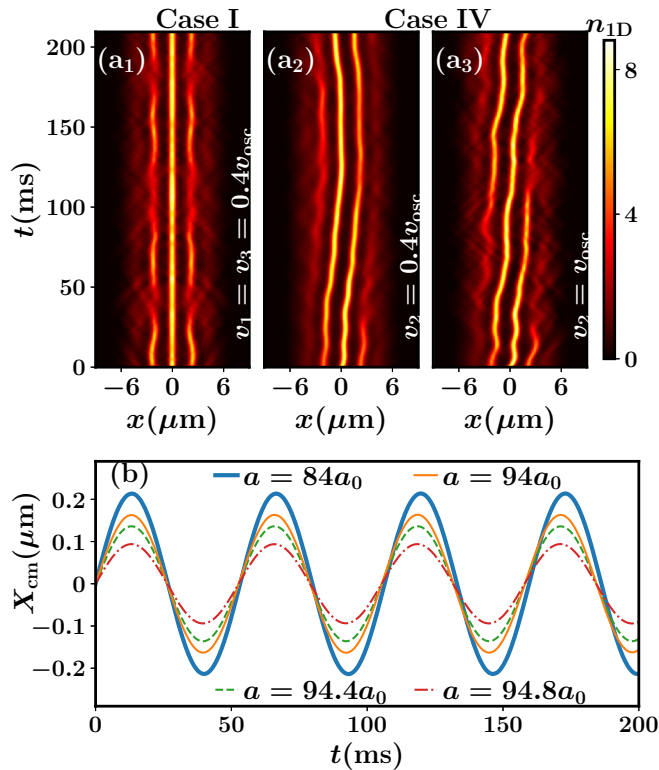


FIG. 4. Time evolution of integrated density n_{1D} within the SS state focusing on (a₁) the case I and (a₂)–(a₃) the case IV for kick velocities $0.4v_{\text{osc}}$ [(a₁), (a₂)] and v_{osc} [(a₃)]. (b) The center-of-mass motion (for case IV) along the x axis for different scattering lengths, $a = 84a_0$ (thick solid line), $a = 94a_0$ (thin solid line), $a = 94.4a_0$ (dashed line) and $a = 94.8a_0$ (dashed dot line) representing varying background density. The colorbar represents the 1D density n_{1D} in units of $1000 \mu\text{m}^{-1}$, and $v_{\text{osc}} = 2.1 \times 10^{-4}$ m/s is the characteristic harmonic oscillator velocity scale.

frequency is determined by the superfluid fraction. This out-of-phase motion decreases both the amplitude and time period of the COM of the entire cloud in the SS state, as determined by the quantity $X_{\text{cm}} = \int x |\psi(x, y, z)|^2 dx dy dz$, see Fig. 4(b). Let us remark that imparting a kick velocity triggers various low-lying excitation modes of the system. The frequency of the COM oscillation in the isolated droplet regime is 19 Hz, which stems from the activation of the so-called dipole mode and is also consistent with the harmonic potential theorem [100]. In the supersolid regime, we find that two modes actually determine the COM. One is again the dipole mode or in-phase Goldstone mode at the trap frequency (consistent with the prediction of the harmonic potential theorem), and the other is the out-of-phase Goldstone mode [11], which is a significantly lower frequency than the trap frequency.¹ This behavior is in line with the fact that isolated droplets can be modeled solely using the classical harmonic oscillator equation, which is unable to capture the vibrational pattern

¹The frequency of the out-of-phase Goldstone mode, calculated by utilizing the Bogoliubov de Gennes analysis [101,102], is 2.17 Hz at $a = 94a_0$.

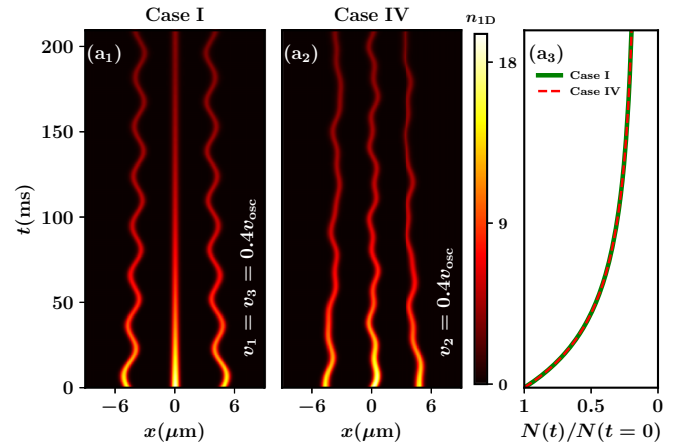


FIG. 5. Time evolution of integrated density n_{1D} of quasi-1D dipolar quantum droplets in the presence of three-body loss focusing on (a₁) case I and (a₂) case II, realized with a kick velocity $0.4v_{\text{osc}}$. Shown also is (a₃) the time evolution of particle number $N(t)$ for two different cases (see the legends). The initial particle number is $N(t=0) = 35000$, and $v_{\text{osc}} = 2.1 \times 10^{-4}$ m/s sets the harmonic oscillator velocity scale. The colorbar represents the density in the unit of $10^3 \mu\text{m}^{-1}$.

of each crystal in the supersolid regime. The alternation of COM mass motion fundamentally serves as an indicator of mass flow and the submergence of classicality in vibrational motion.

VI. IMPACT OF THREE-BODY LOSS

The detection of isolated droplets characterized by highly localized densities is a significant challenge in the experiment due to three-body losses. In the following, we demonstrate the influence of the three-body loss on the previously mentioned vibrational patterns exhibited by isolated droplets. To account for particle loss in our simulation, we introduce a phenomenological three-body term $-i\hbar(L_3/2)|\psi(r)|^4$ into our eGPE [Eq. (1)], where $L_3 = 1.2 \times 10^{-41}$ m⁶/s [33]. We conducted numerical simulations with an initial state of three isolated droplets at a scattering length of $a = 84a_0$ and examined two cases, namely, case I and case IV. The time evolution of the integrated density n_{1D} is analyzed. We observe that, in the presence of the three-body loss term, the amplitude of the out-of-phase vibrational pattern of the two outermost droplets gradually decreased over time [see Fig. 5(a₁)]. However, the vibrational pattern is still captured by underlying vibrational mode \mathbf{A}_3 . The in-phase vibrational pattern of the two outermost droplets in case IV, on the other hand, is disrupted by the three-body term, resulting in the activation of all fundamental modes (\mathbf{A}_1 , \mathbf{A}_2 , \mathbf{A}_3) after $t > 22$ ms. The rate of atom loss, which started at $N(t=0) = 35000$, is found to be independent of the velocity configuration and dependent on the loss rate, L_3 [Fig. 5(a₃)].

Overall, our simulation results demonstrate the ability to capture classical vibrational patterns even in the presence of a three-body loss in isolated droplets. While the current experiments can capture these patterns quantitatively in the early time dynamics, future investigations could extend their

dynamical time span by exploring regions of lower losses in the rich Feshbach spectrum of dysprosium [5].

VII. CONCLUSION

We analyzed the vibrational modes of a linear dipolar droplet array. A selective kicking of isolated droplets induces distinct vibrational patterns resembling those of a classical spring-mass system. At slow kick velocities, a normal mode analysis accurately describes the vibrational patterns. For faster kicks the droplets can touch which may induce a mass flow, so that droplets can coalesce and separate again with different mass distributions, giving rise to different crystalline structures during the dynamics. In the case of a supersolid, classicality is eliminated and a counterflow between droplet motion and superfluid-dilute background occurs. Specifically, our results demonstrate that the classical harmonic oscillator equation accurately characterizes the oscillations of the former, whereas the vibrational patterns of the latter cannot be described by this framework due to the presence of intercrystal superfluid connections. In light of the recent discovery of two-dimensional supersolidity [13,62,65,80] we expect our work to have high relevance for assessing classicality and vibrational modes in these structures. It would be interesting to develop a model that goes beyond the normal mode analysis presented in the article and addresses both the isolated droplets and time-dependent mass transfer in the supersolid regime in a unified manner. It will also be intriguing to compare the normal mode analysis with the underlying collective excitation spectra obtained by a Bogoliubov–de Gennes approach. A finite-temperature study would be equally interesting [103].

ACKNOWLEDGMENTS

This work was financially supported by the Knut and Alice Wallenberg Foundation (Project No. 2018-0217) and the Swedish Research Council (Projects No. 2022-03654_VR and No. 2014-04717_VR). Fruitful discussions with Mikael Nilsson Tengstrand, Tiziano Arnone Cardinale, and Sergej Moroz are acknowledged. We also thank the anonymous referees for their valuable comments.

APPENDIX A: COMPUTATIONAL DETAILS

In our numerical simulations, we cast the extended Gross-Pitaevskii equation (eGP), Eq. (1) in the main article, into a dimensionless form by rescaling the length, the time in terms of the harmonic oscillator lengthscale $l_{\text{osc}} = \sqrt{\hbar/m\omega_x}$, and the trap frequency ω_x , respectively. The wave function is accordingly scaled as $\psi(\mathbf{r}', t) = \sqrt{l_{\text{osc}}^3/N}\psi(\mathbf{r}, t)$. Thereafter we employ split-step Crank-Nicholson method (see [98] in the main article) to solve the resulting dimensionless equation. The stationary (lowest energy) states of the dipolar Bose-Einstein condensate (dBEC) are obtained through imaginary time propagation, effectively a gradient descent algorithm. At each imaginary time step of $\Delta t_i = 10^{-4}/\omega_x$ of this procedure, we apply the transformation $\frac{\psi(\mathbf{r}', t)}{|\psi(\mathbf{r}', t)|} \rightarrow 1$. This preserves the normalization of the wave function, while convergence is reached as long as relative deviations of the wave function (at

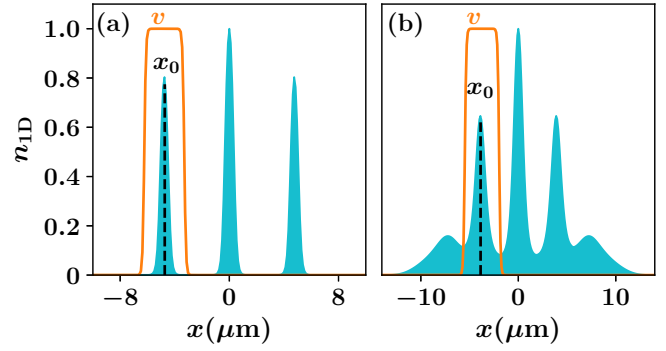


FIG. 6. Shown here are integrated density profiles (blue shaded region), $n_{1D}(z) = \int |\psi(x, y, z)|^2 dx dy$, normalized with respect to the maximum n_{1D} , representing the (a) isolated droplets and (b) supersolid state, realized at $a = 84a_0$ and $a = 94a_0$, respectively. The black dotted lines indicate the central position (x_0) of a droplet crystal. To initiate the dynamics, a droplet is kicked with a velocity v that is constant over the droplet's spatial extension then falls swiftly but continuously to zero.

every grid point) and energy between consecutive time steps are smaller than 10^{-5} and 10^{-7} , respectively. This solution is taken to locate the peak densities and thus identify the central position x_0 of a droplet, see Fig. 6 for the visualization. Subsequently, the wave function is multiplied with the phase $v\mathcal{F}(x)$, where v is the velocity and $\mathcal{F}(x) = A/\{A + B \cosh[L(x - x_0)]\}$ is a modulating function ensuring the continuity of the wave function. We take $A = 10^6$, $B = 0.02$, and L depends on the spatial extension of the droplet along the x axis. Having multiplied the wave function with the above-mentioned phase we propagate the eGP equation in real time to carry out the vibrational and collisional dynamics of dipolar quantum droplets. The simulation is performed in a three-dimensional (3D) box characterized by a grid ($n_x \times n_y \times n_z$) corresponding to $(512 \times 256 \times 256)$ grid points. The employed spatial discretization step is $\Delta x = \Delta y = 0.06l_{\text{osc}}$ and $\Delta z = 0.1l_{\text{osc}}$, while the time step of the numerical integration is $\Delta t = 10^{-5}/\omega_x$. Finally, let us comment that our dynamical simulation is very well resolved up to kick velocity $v = 7.5v_{\text{osc}}$ for the considered spatial discretization steps. However, for stronger kick velocity $v > 7.5v_{\text{osc}}$ since the droplets become very localized during the collision, one should reduce the spatial and temporal discretization steps further. At the same time, one should increase the number of grid points to reduce the boundary effects. The numerical simulation at this velocity scale is expected to be challenging.

APPENDIX B: DETAILED DERIVATION OF THE NORMAL MODES OF VIBRATION

As we explicated in the main text, the vibrational motion of the three isolated quantum droplets can be modeled by resorting to a spring-mass system [88], where three masses are connected by the springs with the identical spring constant k [see Fig. 1(c) in the main text]. The x_1 , x_2 , and x_3 denote the displacement of the left, center, and right masses from their equilibrium positions. To correctly capture the physical situation, we consider that $m_1 = m_2 = m$. Assuming that the

spring force is linear, the equations of motion of three masses can be written as

$$m\ddot{x}_1 = -kx_1 - k(x_1 - x_2), \quad (\text{B1})$$

$$m_2\ddot{x}_2 = -k(x_2 - x_1) - k(x_2 - x_3), \quad (\text{B2})$$

$$m\ddot{x}_3 = -k(x_3 - x_2) - kx_3. \quad (\text{B3})$$

From Eqs. (B1), (B2), and (B3), we get

$$\ddot{x}_1 = -\omega_1^2 x_1 - \omega_1^2 (x_1 - x_2), \quad (\text{B4})$$

$$\ddot{x}_2 = -\omega_2^2 (x_2 - x_1) - \omega_2^2 (x_2 - x_3), \quad (\text{B5})$$

$$\ddot{x}_3 = -\omega_1^2 (x_3 - x_2) - \omega_1^2 x_3, \quad (\text{B6})$$

where $\omega_1 = \sqrt{k/m}$, $\omega_2 = \sqrt{k/m_2}$. The solution of Eqs. (B4), (B5), and (B6) can be written in the form $x_j = \mathcal{A}_j e^{i\omega t}$. This gives the set of equations

$$\mathcal{A}_1(\omega^2 - 2\omega_1^2) + \omega_1^2 \mathcal{A}_2 = 0, \quad (\text{B7})$$

$$\omega_2^2 \mathcal{A}_1 + \mathcal{A}_2(\omega^2 - 2\omega_2^2) + \omega_2^2 \mathcal{A}_3 = 0, \quad (\text{B8})$$

and

$$\omega_1^2 \mathcal{A}_2 + (\omega^2 - 2\omega_1^2) \mathcal{A}_3 = 0. \quad (\text{B9})$$

The above equations can be cast into a matrix of the form $\mathbf{M}\mathbf{A} = 0$, where

$$\mathbf{M} = \begin{pmatrix} \omega^2 - 2\omega_1^2 & \omega_1^2 & 0 \\ \omega_2^2 & \omega^2 - 2\omega_2^2 & \omega_2^2 \\ 0 & \omega_1^2 & \omega^2 - 2\omega_1^2 \end{pmatrix}, \quad (\text{B10})$$

and

$$\mathbf{A} = \begin{pmatrix} \mathcal{A}_1 \\ \mathcal{A}_2 \\ \mathcal{A}_3 \end{pmatrix}. \quad (\text{B11})$$

A nonzero solution exist for \mathbf{A} only if the determinant of \mathbf{M} is zero. This gives

$$(\omega^2 - 2\omega_1^2)[(\omega^2 - 2\omega_2^2)(\omega^2 - 2\omega_1^2) - \omega_1^2 \omega_2^2] - \omega_1^2 \omega_2^2 (\omega^2 - 2\omega_1^2) = 0. \quad (\text{B12})$$

The roots of the Eq. (B12) are $\omega^2 = 2\omega_1^2$ and $\omega^2 = \omega_1^2 + \omega_2^2 \pm \sqrt{\omega_1^4 + \omega_2^4}$. Plugging these values back into Eq. (B10) we can determine the relations between \mathcal{A}_1 , \mathcal{A}_2 , and \mathcal{A}_3 , which gives the three normal modes, $\mathcal{A}_1 : \mathcal{A}_2 : \mathcal{A}_3 = \omega_1^2 : \omega^2 - 2\omega_1^2 : \omega_1^2$. For $\omega = \omega_m = \pm\sqrt{2}\omega_1$, the eigenmode is

$$\mathbf{A}_1 = \begin{pmatrix} \mathcal{A}_1 \\ \mathcal{A}_2 \\ \mathcal{A}_3 \end{pmatrix} = \begin{pmatrix} \omega_1^2 \\ 0 \\ -\omega_1^2 \end{pmatrix}. \quad (\text{B13})$$

For $\omega = \omega_f = \pm[\omega_1^2 + \omega_2^2 + \sqrt{\omega_1^4 + \omega_2^4}]^{1/2}$, the eigenmode reads

$$\mathbf{A}_2 = \begin{pmatrix} \mathcal{A}_1 \\ \mathcal{A}_2 \\ \mathcal{A}_3 \end{pmatrix} = \begin{pmatrix} \omega_1^2 \\ \omega_-^2 \\ \omega_1^2 \end{pmatrix}. \quad (\text{B14})$$

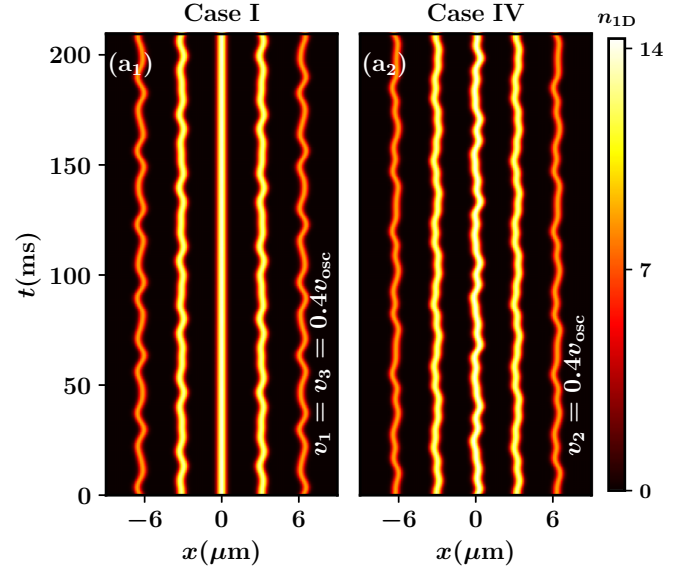


FIG. 7. Time evolution of integrated density n_{1D} of quasi-1D dipolar quantum droplets featuring five localized isolated crystal structures, considering case I and case IV. The initial state of the system consists of $N = 45000$ atoms in a harmonic trapping potential with frequencies $(\omega_x, \omega_y, \omega_z)/(2\pi) = (33, 100, 167)$ Hz and scattering length $a = 79a_0$. The characteristic harmonic oscillator velocity scale of the system is $v_{osc} = 4.56 \times 10^{-4}$ m/s. The colorbar represents the density in the unit of $10^3 \mu\text{m}^{-1}$.

Finally, for $\omega = \omega_s = \pm[\omega_1^2 + \omega_2^2 - \sqrt{\omega_1^4 + \omega_2^4}]^{1/2}$, the eigenmode becomes

$$\mathbf{A}_3 = \begin{pmatrix} \mathcal{A}_1 \\ \mathcal{A}_2 \\ \mathcal{A}_3 \end{pmatrix} = \begin{pmatrix} \omega_1^2 \\ \omega_+^2 \\ \omega_1^2 \end{pmatrix}. \quad (\text{B15})$$

Here, $\omega_{\pm}^2 = (\omega_2^2 - \omega_1^2) \pm \sqrt{\omega_1^4 + \omega_2^4}$.

Thus, the most general solution $\mathbf{X} = (x_1, x_2, x_3)$ can be written as

$$\mathbf{X} = a_m \mathbf{A}_1 \cos(\omega_m t + \phi_m) + a_f \mathbf{A}_2 \cos(\omega_f t + \phi_f) + a_s \mathbf{A}_3 \cos(\omega_s t + \phi_s). \quad (\text{B16})$$

The six unknowns, a_m , a_s , a_f , ϕ_m , ϕ_f , and ϕ_s are determined by the six initial conditions (three positions and three velocities). In the following for all the cases considered we fixed the initial conditions on the positions, namely, $x_1 = 0$, $x_2 = 0$, and $x_3 = 0$. This gives $\phi_m = \phi_f = \phi_s = \pi/2$.

APPENDIX C: VIBRATIONAL PATTERN OF FIVE ISOLATED DROPLETS

In the main text, our focus has been primarily on the vibrational dynamics of the three-droplet state. Here, we present a system consisting of five localized isolated droplets [80], created within a harmonic trapping potential with $(\omega_x, \omega_y, \omega_z)/(2\pi) = (33, 100, 167)$ Hz by $N = 45000$ dysprosium atoms having scattering length $a = 79a_0$. This system possesses five normal mode frequencies. While a thorough analysis of this system through numerical simulation and normal mode analysis, akin to that of the three-droplet

systems, is outside the scope of this work, we demonstrate two specific cases that resemble case **I** and case **IV** of the three-droplet systems. In the first (case **I**), equal magnitude kicks are given to the outermost droplets (of five-droplet configurations) in opposite directions. In the second (case **IV**), only the central droplet is kicked in the $+x$ direction. Figs. 7(a₁) and 7(a₂) show the time evolution of the $n_{1D}(x)$ density for case **I** and case **IV**, respectively.

For case **I**, we observe that the first and fifth droplets exhibit out-of-phase vibrational patterns, while the central

(third) droplet remains motionless. This behavior is highly reminiscent of case **I** in the three-droplet configuration. In case **IV**, as shown in Fig. 7(a₂), the first and fifth droplets demonstrate in-phase motion (as do the second and fourth droplets), indicating a striking similarity to case **IV** in the three-droplet configuration.

These findings demonstrate that the analysis detailed in the main text can be extended to systems containing any number of droplets and provide further insight into the vibrational dynamics of quasi-one-dimensional dipolar quantum droplets.

-
- [1] M. Baranov, *Phys. Rep.* **464**, 71 (2008).
- [2] T. Lahaye, C. Menotti, L. Santos, M. Lewenstein, and T. Pfau, *Rep. Prog. Phys.* **72**, 126401 (2009).
- [3] M. A. Baranov, M. Dalmonte, G. Pupillo, and P. Zoller, *Chem. Rev.* **112**, 5012 (2012).
- [4] F. Böttcher, J.-N. Schmidt, J. Hertkorn, K. S. H. Ng, S. D. Graham, M. Guo, T. Langen, and T. Pfau, *Rep. Prog. Phys.* **84**, 012403 (2021).
- [5] L. Chomaz, I. Ferrier-Barbut, F. Ferlaino, B. Laburthe-Tolra, B. L. Lev, and T. Pfau, *Rep. Prog. Phys.* **86**, 026401 (2023).
- [6] F. Böttcher, J.-N. Schmidt, M. Wenzel, J. Hertkorn, M. Guo, T. Langen, and T. Pfau, *Phys. Rev. X* **9**, 011051 (2019).
- [7] L. Tanzi, E. Lucioni, F. Famà, J. Catani, A. Fioretti, C. Gabbanini, R. N. Bisset, L. Santos, and G. Modugno, *Phys. Rev. Lett.* **122**, 130405 (2019).
- [8] L. Chomaz, D. Petter, P. Ilzhöfer, G. Natale, A. Trautmann, C. Politi, G. Durastante, R. M. W. van Bijnen, A. Patscheider, M. Sohmen, M. J. Mark, and F. Ferlaino, *Phys. Rev. X* **9**, 021012 (2019).
- [9] G. Natale, R. M. W. van Bijnen, A. Patscheider, D. Petter, M. J. Mark, L. Chomaz, and F. Ferlaino, *Phys. Rev. Lett.* **123**, 050402 (2019).
- [10] L. Tanzi, S. M. Rocuzzo, E. Lucioni, F. Fama, A. Fioretti, C. Gabbanini, G. Modugno, A. Recati, and S. Stringari, *Nature (London)* **574**, 382 (2019).
- [11] M. Guo, F. Böttcher, J. Hertkorn, J.-N. Schmidt, M. Wenzel, H. P. Büchler, T. Langen, and T. Pfau, *Nature (London)* **574**, 386 (2019).
- [12] J. Hertkorn, F. Böttcher, M. Guo, J. N. Schmidt, T. Langen, H. P. Büchler, and T. Pfau, *Phys. Rev. Lett.* **123**, 193002 (2019).
- [13] J. Hertkorn, J.-N. Schmidt, M. Guo, F. Böttcher, K. S. H. Ng, S. D. Graham, P. Uerlings, H. P. Büchler, T. Langen, M. Zwierlein, and T. Pfau, *Phys. Rev. Lett.* **127**, 155301 (2021).
- [14] E. P. Gross, *Phys. Rev.* **106**, 161 (1957); *Ann. Phys. (N.Y.)* **4**, 57 (1958).
- [15] C. N. Yang, *Rev. Mod. Phys.* **34**, 694 (1962).
- [16] A. Andreev and I. Lifshits, *Zh. Eksp. Teor. Fiz.* **56**, 2057 (1969) [*Sov. Phys.-JETP* **29**, 1107 (1969)].
- [17] G. V. Chester, *Phys. Rev. A* **2**, 256 (1970).
- [18] A. J. Leggett, *Phys. Rev. Lett.* **25**, 1543 (1970).
- [19] Y. Pomeau and S. Rica, *Phys. Rev. Lett.* **72**, 2426 (1994).
- [20] M. Boninsegni and N. V. Prokof'ev, *Rev. Mod. Phys.* **84**, 759 (2012).
- [21] E. Kim and M. H. W. Chan, *Nature (London)* **427**, 225 (2004); *Science* **305**, 1941 (2004).
- [22] S. Balibar, *Nature (London)* **464**, 176 (2010).
- [23] D. Y. Kim and M. H. W. Chan, *Phys. Rev. Lett.* **109**, 155301 (2012).
- [24] M. H. W. Chan, R. B. Hallock, and L. Reatto, *J. Low Temp. Phys.* **172**, 317 (2013).
- [25] N. Henkel, R. Nath, and T. Pohl, *Phys. Rev. Lett.* **104**, 195302 (2010).
- [26] F. Cinti, P. Jain, M. Boninsegni, A. Micheli, P. Zoller, and G. Pupillo, *Phys. Rev. Lett.* **105**, 135301 (2010).
- [27] S. Saccani, S. Moroni, and M. Boninsegni, *Phys. Rev. B* **83**, 092506 (2011).
- [28] J. Léonard, A. Morales, P. Zupancic, T. Donner, and T. Esslinger, *Science* **358**, 1415 (2017); J. Léonard, A. Morales, P. Zupancic, T. Esslinger, and T. Donner, *Nature (London)* **543**, 87 (2017).
- [29] Y. J. Lin, K. Jiménez-García, and I. B. Spielman, *Nature (London)* **471**, 83 (2011).
- [30] J. R. Li, W. Huang, B. Shteynas, S. Burchesky, F. C. Top, E. Su, J. Lee, A. O. Jamison, and W. Ketterle, *Phys. Rev. Lett.* **117**, 185301 (2016).
- [31] J.-R. Li, J. Lee, W. Huang, S. Burchesky, B. Shteynas, F. C. Top, A. O. Jamison, and W. Ketterle, *Nature (London)* **543**, 91 (2017).
- [32] A. R. P. Lima and A. Pelster, *Phys. Rev. A* **84**, 041604(R) (2011).
- [33] F. Wächtler and L. Santos, *Phys. Rev. A* **93**, 061603(R) (2016); **94**, 043618 (2016).
- [34] R. N. Bisset, R. M. Wilson, D. Baillie, and P. B. Blakie, *Phys. Rev. A* **94**, 033619 (2016).
- [35] H. Kadau, M. Schmitt, M. Wenzel, C. Wink, T. Maier, I. Ferrier-Barbut, and T. Pfau, *Nature (London)* **530**, 194 (2016).
- [36] I. Ferrier-Barbut, H. Kadau, M. Schmitt, M. Wenzel, and T. Pfau, *Phys. Rev. Lett.* **116**, 215301 (2016).
- [37] M. Schmitt, M. Wenzel, F. Böttcher, I. Ferrier-Barbut, and T. Pfau, *Nature (London)* **539**, 259 (2016).
- [38] F. Böttcher, M. Wenzel, J.-N. Schmidt, M. Guo, T. Langen, I. Ferrier-Barbut, T. Pfau, R. Bombín, J. Sánchez-Baena, J. Boronat, and F. Mazzanti, *Phys. Rev. Res.* **1**, 033088 (2019).
- [39] L. Chomaz, S. Baier, D. Petter, M. J. Mark, F. Wächtler, L. Santos, and F. Ferlaino, *Phys. Rev. X* **6**, 041039 (2016).
- [40] L. Chomaz, R. M. W. van Bijnen, D. Petter, G. Faraoni, S. Baier, J. H. Becher, M. J. Mark, F. Wächtler, L. Santos, and F. Ferlaino, *Nat. Phys.* **14**, 442 (2018).
- [41] D. S. Petrov, *Phys. Rev. Lett.* **115**, 155302 (2015).
- [42] D. S. Petrov and G. E. Astrakharchik, *Phys. Rev. Lett.* **117**, 100401 (2016).

- [43] N. B. Jørgensen, G. M. Bruun, and J. J. Arlt, *Phys. Rev. Lett.* **121**, 173403 (2018).
- [44] C. R. Cabrera, L. Tanzi, J. Sanz, B. Naylor, P. Thomas, P. Cheiney, and L. Tarruell, *Science* **359**, 301 (2018).
- [45] G. Semeghini, G. Ferioli, L. Masi, C. Mazzinghi, L. Wolswijk, F. Minardi, M. Modugno, G. Modugno, M. Inguscio, and M. Fattori, *Phys. Rev. Lett.* **120**, 235301 (2018).
- [46] T. G. Skov, M. G. Skou, N. B. Jørgensen, and J. J. Arlt, *Phys. Rev. Lett.* **126**, 230404 (2021).
- [47] S. M. Roccuzzo and F. Ancilotto, *Phys. Rev. A* **99**, 041601(R) (2019).
- [48] R. N. Bisset and P. B. Blakie, *Phys. Rev. A* **92**, 061603(R) (2015).
- [49] K.-T. Xi and H. Saito, *Phys. Rev. A* **93**, 011604(R) (2016).
- [50] P. B. Blakie, *Phys. Rev. A* **93**, 033644 (2016).
- [51] H. Saito, *J. Phys. Soc. Jpn.* **85**, 053001 (2016).
- [52] A. Macia, J. Sánchez-Baena, J. Boronat, and F. Mazzanti, *Phys. Rev. Lett.* **117**, 205301 (2016).
- [53] D. Baillie, R. M. Wilson, and P. B. Blakie, *Phys. Rev. Lett.* **119**, 255302 (2017).
- [54] D. Edler, C. Mishra, F. Wächtler, R. Nath, S. Sinha, and L. Santos, *Phys. Rev. Lett.* **119**, 050403 (2017).
- [55] D. Baillie and P. B. Blakie, *Phys. Rev. Lett.* **121**, 195301 (2018).
- [56] Y.-C. Zhang, F. Maucher, and T. Pohl, *Phys. Rev. Lett.* **123**, 015301 (2019).
- [57] P. B. Blakie, D. Baillie, L. Chomaz, and F. Ferlaino, *Phys. Rev. Res.* **2**, 043318 (2020).
- [58] S. M. Roccuzzo, A. Gallemí, A. Recati, and S. Stringari, *Phys. Rev. Lett.* **124**, 045702 (2020).
- [59] A. Gallemí, S. M. Roccuzzo, S. Stringari, and A. Recati, *Phys. Rev. A* **102**, 023322 (2020).
- [60] C. Mishra, L. Santos, and R. Nath, *Phys. Rev. Lett.* **124**, 073402 (2020).
- [61] L. Chomaz, *Phys. Rev. A* **102**, 023333 (2020).
- [62] E. Poli, T. Bland, C. Politi, L. Klaus, M. A. Norcia, F. Ferlaino, R. N. Bisset, and L. Santos, *Phys. Rev. A* **104**, 063307 (2021).
- [63] J. Hertkorn, J.-N. Schmidt, M. Guo, F. Böttcher, K. S. H. Ng, S. D. Graham, P. Uerlings, T. Langen, M. Zwierlein, and T. Pfau, *Phys. Rev. Res.* **3**, 033125 (2021).
- [64] Y.-C. Zhang, T. Pohl, and F. Maucher, *Phys. Rev. A* **104**, 013310 (2021).
- [65] T. Bland, E. Poli, C. Politi, L. Klaus, M. A. Norcia, F. Ferlaino, L. Santos, and R. N. Bisset, *Phys. Rev. Lett.* **128**, 195302 (2022).
- [66] L. E. Young-S. and S. K. Adhikari, *Phys. Rev. A* **105**, 033311 (2022).
- [67] R. Ghosh, C. Mishra, L. Santos, and R. Nath, *Phys. Rev. A* **106**, 063318 (2022).
- [68] A. Gallemí and L. Santos, *Phys. Rev. A* **106**, 063301 (2022).
- [69] M. Schmidt, L. Lassablière, G. Quémener, and T. Langen, *Phys. Rev. Res.* **4**, 013235 (2022).
- [70] S. Halder, K. Mukherjee, S. I. Mistakidis, S. Das, P. G. Kevrekidis, P. K. Panigrahi, S. Majumder, and H. R. Sadeghpour, *Phys. Rev. Res.* **4**, 043124 (2022).
- [71] M. N. Tengstrand, D. Boholm, R. Sachdeva, J. Bengtsson, and S. M. Reimann, *Phys. Rev. A* **103**, 013313 (2021).
- [72] S. M. Roccuzzo, A. Recati, and S. Stringari, *Phys. Rev. A* **105**, 023316 (2022).
- [73] M. Šindik, A. Recati, S. M. Roccuzzo, L. Santos, and S. Stringari, *Phys. Rev. A* **106**, L061303 (2022).
- [74] J. C. Smith, D. Baillie, and P. B. Blakie, *Phys. Rev. Lett.* **126**, 025302 (2021).
- [75] R. N. Bisset, L. A. Pena Ardila, and L. Santos, *Phys. Rev. Lett.* **126**, 025301 (2021).
- [76] S. Li, U. N. Le, and H. Saito, *Phys. Rev. A* **105**, L061302 (2022).
- [77] D. Scheiermann, L. A. Pena Ardila, T. Bland, R. N. Bisset, and L. Santos, *Phys. Rev. A* **107**, L021302 (2023).
- [78] T. Bland, E. Poli, L. A. Peña Ardila, L. Santos, F. Ferlaino, and R. N. Bisset, *Phys. Rev. A* **106**, 053322 (2022).
- [79] S. Halder, S. Das, and S. Majumder, [arXiv:2210.00598](https://arxiv.org/abs/2210.00598).
- [80] M. A. Norcia, C. Politi, L. Klaus, E. Poli, M. Sohmen, M. J. Mark, R. N. Bisset, L. Santos, and F. Ferlaino, *Nature (London)* **596**, 357 (2021).
- [81] J.-N. Schmidt, J. Hertkorn, M. Guo, F. Böttcher, M. Schmidt, K. S. H. Ng, S. D. Graham, T. Langen, M. Zwierlein, and T. Pfau, *Phys. Rev. Lett.* **126**, 193002 (2021).
- [82] G. Biagioni, N. Antolini, A. Alaña, M. Modugno, A. Fioretti, C. Gabbanini, L. Tanzi, and G. Modugno, *Phys. Rev. X* **12**, 021019 (2022).
- [83] L. Klaus, T. Bland, E. Poli, C. Politi, G. Lamporesi, E. Casotti, R. N. Bisset, M. J. Mark, and F. Ferlaino, *Nat. Phys.* **18**, 1453 (2022).
- [84] M. Sohmen, C. Politi, L. Klaus, L. Chomaz, M. J. Mark, M. A. Norcia, and F. Ferlaino, *Phys. Rev. Lett.* **126**, 233401 (2021).
- [85] P. Ilzhöfer, M. Sohmen, G. Durastante, C. Politi, A. Trautmann, G. Natale, G. Morpurgo, T. Giamarchi, L. Chomaz, M. J. Mark, and F. Ferlaino, *Nat. Phys.* **17**, 356 (2021).
- [86] M. A. Norcia, E. Poli, C. Politi, L. Klaus, T. Bland, M. J. Mark, L. Santos, R. N. Bisset, and F. Ferlaino, *Phys. Rev. Lett.* **129**, 040403 (2022).
- [87] D. E. Rutherford, *Classical Mechanics* (Oliver and Boyd, Edinburgh, Scotland, 1967).
- [88] A. B. Pippard, *The Physics of Vibrations* (Cambridge University Press, Cambridge, England, 1978).
- [89] N. Ashgriz and J. Y. Poo, *J. Fluid Mech.* **221**, 183 (1990).
- [90] J. Qian and C. K. Law, *J. Fluid Mech.* **331**, 59 (1997).
- [91] B. Turmanov, B. Baizakov, B. Umarov, and F. Abdullaev, *Phys. Lett. A* **379**, 1828 (2015).
- [92] B. B. Baizakov, S. M. Al-Marzoug, and H. Bahlouli, *Phys. Rev. A* **92**, 033605 (2015).
- [93] M. Salerno and B. B. Baizakov, *Phys. Rev. E* **98**, 062220 (2018).
- [94] G. Ferioli, G. Semeghini, L. Masi, G. Giusti, G. Modugno, M. Inguscio, A. Gallemí, A. Recati, and M. Fattori, *Phys. Rev. Lett.* **122**, 090401 (2019).
- [95] V. Cikojević, L. V. C. V. Markić, M. Pi, M. Barranco, F. Ancilotto, and J. Boronat, *Phys. Rev. Res.* **3**, 043139 (2021).

- [96] J. E. Alba-Arroyo, S. F. Caballero-Benitez, and R. Jáuregui, *Sci. Rep.* **12**, 18467 (2022).
- [97] A. R. P. Lima and A. Pelster, *Phys. Rev. A* **86**, 063609 (2012).
- [98] J. Crank and P. Nicolson, *Math. Proc. Cambridge Philos. Soc.* **43**, 50 (1947).
- [99] X. Antoine, W. Bao, and C. Besse, *Comput. Phys. Commun.* **184**, 2621 (2013).
- [100] J. F. Dobson, *Phys. Rev. Lett.* **73**, 2244 (1994).
- [101] C. J. Pethick and H. Smith, *Bose-Einstein Condensation in Dilute Gases* (Cambridge University Press, Cambridge, England, 2002).
- [102] S. Stringari and L. Pitaevskii, *Bose-Einstein Condensation* (Oxford University Press, Oxford, 2003).
- [103] J. Sánchez-Baena, C. Politi, F. Maucher, F. Ferlaino, and T. Pohl, *Nat. Commun.* **14**, 1868 (2023).